

The solar dynamo begins near the surface

<https://doi.org/10.1038/s41586-024-07315-1>

Received: 19 August 2023

Accepted: 14 March 2024

Published online: 22 May 2024

Open access

 Check for updates

Geoffrey M. Vasil^{1✉}, Daniel Lecoanet^{2,3}, Kyle Augustson^{2,3}, Keaton J. Burns^{4,5}, Jeffrey S. Oishi⁶, Benjamin P. Brown⁷, Nicholas Brummell⁸ & Keith Julien^{9,10}

The magnetic dynamo cycle of the Sun features a distinct pattern: a propagating region of sunspot emergence appears around 30° latitude and vanishes near the equator every 11 years (ref. 1). Moreover, longitudinal flows called torsional oscillations closely shadow sunspot migration, undoubtedly sharing a common cause². Contrary to theories suggesting deep origins of these phenomena, helioseismology pinpoints low-latitude torsional oscillations to the outer 5–10% of the Sun, the near-surface shear layer^{3,4}. Within this zone, inwardly increasing differential rotation coupled with a poloidal magnetic field strongly implicates the magneto-rotational instability^{5,6}, prominent in accretion-disk theory and observed in laboratory experiments⁷. Together, these two facts prompt the general question: whether the solar dynamo is possibly a near-surface instability. Here we report strong affirmative evidence in stark contrast to traditional models⁸ focusing on the deeper tachocline. Simple analytic estimates show that the near-surface magneto-rotational instability better explains the spatiotemporal scales of the torsional oscillations and inferred subsurface magnetic field amplitudes⁹. State-of-the-art numerical simulations corroborate these estimates and reproduce hemispherical magnetic current helicity laws¹⁰. The dynamo resulting from a well-understood near-surface phenomenon improves prospects for accurate predictions of full magnetic cycles and space weather, affecting the electromagnetic infrastructure of Earth.

Key observations that any model must take into account include (1) the solar butterfly diagram, a decadal migration pattern of sunspot emergence^{1,4} with strong latitude dependence; (2) the torsional oscillations constituting local rotation variations corresponding with magnetic activity^{2–4}; (3) the poloidal field, an approximately 1 G photospheric field with a 1/4-cycle phase lag relative to sunspots¹¹, and approximately 100 G subsurface amplitudes⁹; (4) the hemispherical helicity sign rule comprising an empirically observed negative current helicity in the northern hemisphere and positive current helicity in the south¹⁰; (5) the tachocline at the base of the convection zone, the traditionally proposed seat of the solar dynamo; and (6) the near-surface-shear layer (NSSL) within the outer 5–10% of the Sun containing strong inwardly increasing angular velocity fostering the magneto-rotational instability (MRI).

Despite progress, prevailing theories have distinct limitations. Interface dynamos (proposed within the tachocline⁸) preferentially generate high-latitude fields¹² and produce severe shear disruptions¹³ that are not observed¹⁴. Mean-field dynamos offer qualitative insights but suffer from the absence of first principles¹⁵ and are contradicted by observed meridional circulations¹⁶. Global convection-zone models often misalign with important solar observations, require conditions diverging from solar reality^{17–19} and fail to provide a theoretical dynamical understanding.

Borrowing from well-established ideas in accretion-disk physics^{5,6}, we propose an alternative hypothesis that produces clear predictions and quantitatively matches key observations.

For electrically conducting plasma such as the Sun, the local axisymmetric linear instability criterion for the MRI is^{5,6}

$$2QS > \omega_A^2, \quad (1)$$

where the local Alfvén frequency and shear are

$$\omega_A = \frac{B_0 k_r}{\sqrt{4\pi\rho_0}} \text{ and } S = -r \frac{d\Omega}{dr}. \quad (2)$$

The system control parameters are the background poloidal magnetic field strength (B_0 in cgs units), the atmospheric density (ρ_0), the smallest non-trivial radial wavenumber that will fit in the domain ($k_r \approx \pi/H_r$, where H_r is a relevant layer depth or density-scale height), bulk rotation rate (Ω) and the differential rotation, or shear ($S > 0$ in the NSSL). An adiabatic density stratification holds to a good approximation within the solar convection zone, eliminating buoyancy modifications to the stability condition in equation (1).

The MRI is essential for generating turbulent angular momentum transport in magnetized astrophysical disks⁶. Previous work²⁰ postulated the NSSL as the possible seat of the global dynamo without invoking the MRI. A kinematic dynamo study²¹ dismissed the relevance of NSSL but did not allow for full magnetohydrodynamic (MHD) instabilities (such as the MRI). Modern breakthroughs in our understanding of large-scale MRI physics^{22,23} have not been applied in a solar context,

¹School of Mathematics and the Maxwell Institute for Mathematical Sciences, University of Edinburgh, Edinburgh, UK. ²Department of Engineering Sciences and Applied Mathematics, Northwestern University, Evanston, IL, USA. ³CIERA, Northwestern University, Evanston, IL, USA. ⁴Department of Mathematics, Massachusetts Institute of Technology, Cambridge, MA, USA. ⁵Center for Computational Astrophysics, Flatiron Institute, New York, NY, USA. ⁶Department of Physics and Astronomy, Bates College, Lewiston, ME, USA. ⁷Department of Astrophysical and Planetary Sciences, University of Colorado Boulder, Boulder, CO, USA. ⁸Department of Applied Mathematics, Jack Baskin School of Engineering, University of California Santa Cruz, Santa Cruz, CA, USA. ⁹Department of Applied Mathematics, University of Colorado Boulder, Boulder, CO, USA. ¹⁰Deceased: Keith Julien. ✉e-mail: gvasil@ed.ac.uk

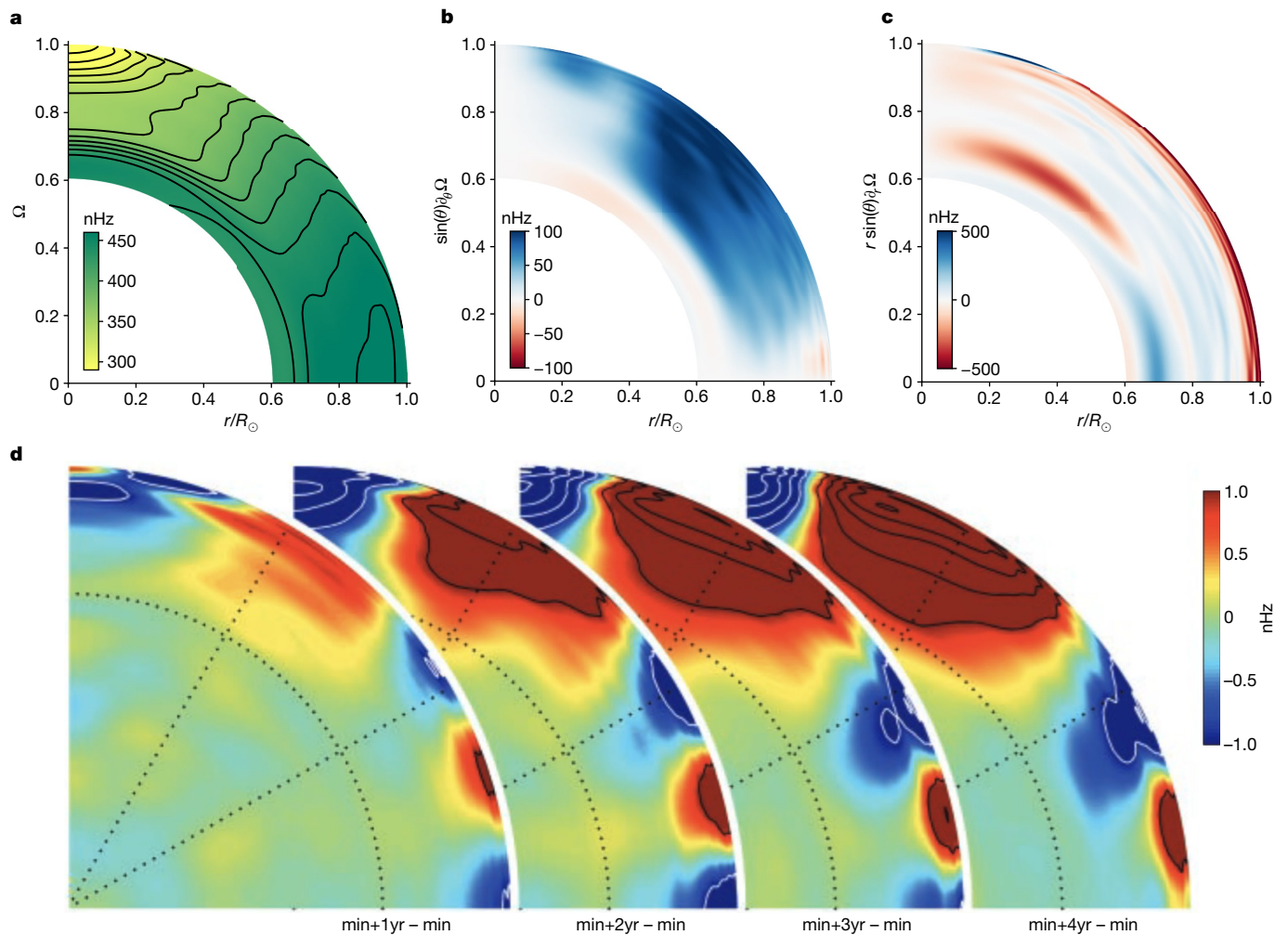


Fig. 1 | Measured internal solar rotation profiles. **a**, Helioseismic differential rotation profile, $\Omega(\theta, r)$ using publicly available data from ref. 29. **b,c**, The respective latitudinal and radial shear gradients $r \sin(\theta) \nabla \Omega(\theta, r)$ computed by a non-uniform fourth-order centred finite-difference scheme. The latitudinal mean of tachocline shear is about 200 nHz and peak amplitudes are below about 350 nHz. Conversely, the near-surface shear averages about 400–600 nHz (with rapid variation in depth) and peak values average around 1,200 nHz. **d**, Helioseismic measurements of solar torsional oscillations. The red shows

positive residual rotation rates and blue shows negative residual rotation rates after removing the 1996 annual mean of $\Omega(r, \theta)$. Each slice shows the rotational perturbations 1, 2, 3 and 4 years after the approximate solar minimum. The notation ‘min+1yr – min’ means taking the profile at 1 year past solar minimum and subtracting the profile at solar minimum. The colour table saturates at ± 1 nHz, corresponding to about 400 cm s^{-1} surface flow amplitude. Further contour lines show 1 nHz increments within the saturated regions. Diagram in **d** reproduced with permission from figure 2 in ref. 3, AAAS.

and local MRI studies of the Sun²⁴ have considered only small scales. To our knowledge, no work has yet considered large-scale MRI dynamics relevant to the observed features of the global dynamo. We therefore describe here a potential MRI-driven solar dynamo cycle.

The start of the solar cycle is the period surrounding the sunspot minimum when there is no significant toroidal field above the equator and a maximal poloidal field below the photosphere. This configuration is unstable to the axisymmetric MRI, which generates a dynamically active toroidal field in the outer convection zone. The observed torsional oscillations are the longitudinal flow perturbations arising from the MRI. The relative energetics are consistent with nonlinear dynamo estimates (Methods). As the cycle progresses, the toroidal field can undergo several possible MHD instabilities contributing to poloidal-field regeneration, for example, the helical MRI, non-axis-symmetric MRI, the clamshell instability and several more, including a surface Babcock–Leighton process. We propose that the axisymmetric subsurface field and torsional oscillations constitute a nonlinear MRI travelling wave. The instability saturates by radial transport of (globally conserved) mean magnetic flux (B_0) and angular

momentum (Ω, S), which neutralize the instability criterion in equation (1) (Methods).

Empirical timescales of the torsional oscillations imply an approximate growth rate, γ , for the MRI and, therefore, a relevant poloidal field strength. To a good approximation, $S \approx \Omega \approx 2\pi/\text{month}$ in the NSSL (Fig. 1a–c). The early-phase torsional oscillations change on a timescale of 2–12 months, implying a growth rate of $\gamma/\Omega \approx 0.01\text{--}0.1$ (Methods). A modest growth rate and the regularity of the solar cycle over long intervals together suggest that the global dynamics operate in a mildly nonlinear regime. Altogether, we predict roughly $\omega_A \approx S \approx \Omega$.

The torsional oscillation pattern shows an early-phase mode-like structure with an approximately 4:1 horizontal aspect ratio occupying a depth of roughly $r/R_\odot \approx 5\%$, or $k_r \approx 70 R_\odot^{-1}$ (Fig. 1d). Using equation (2), the approximate background Alfvén speed $v_A \approx 200\text{--}2,000 \text{ cm s}^{-1} \approx 0.1\text{--}1.0 R_\odot/\text{year}$.

Alfvén-speed estimates required for MRI dynamics are consistent with observed internal magnetic field strengths. Measurements suggest 100–200 G internal poloidal field⁹, agreeing with the above estimates using NSSL densities $\rho_0 \approx 3 \times 10^{-2} \text{ g cm}^{-3}$ to $3 \times 10^{-4} \text{ g cm}^{-3}$. The same

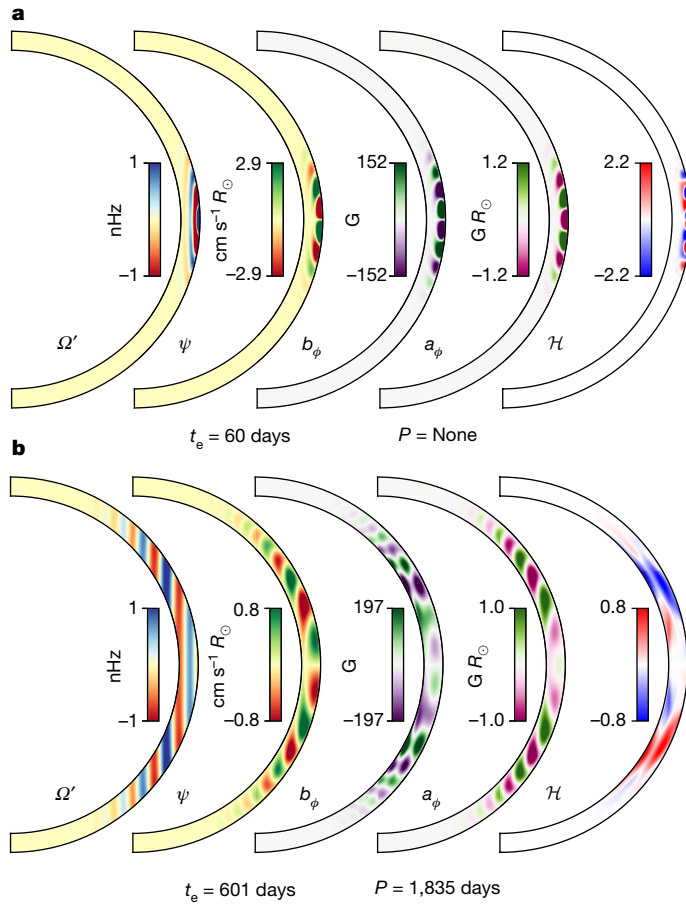


Fig. 2 | Two meridional (r, θ) MRI eigenmode profiles. Longitudinal angular velocity perturbation, $\Omega'(r, \theta) = u_\phi(r, \theta)/(r \sin \theta)$; momentum-density streamfunction (ϕ -directed component; Methods), $\psi(r, \theta)$; longitudinal magnetic field, $b_\phi(r, \theta)$; magnetic scalar potential, $a_\phi(r, \theta)$; and current helicity correlation, $\mathcal{H}(r, \theta)$. The timescales t_e and P represent the instability e-folding time and oscillation period, respectively. **a**, Case 1: a typical directly growing fast-branch mode with no oscillation and growth rates $\gamma \approx 0.06\Omega_0$. **b**, Case 2: a typical large-scale slow-branch mode with a roughly 5-year period. In each case, we fix the overall amplitude to 1 nHz for the rotational perturbations, with all other quantities taking their corresponding relative values.

studies found roughly similar (300–1,000 G) internal toroidal field strength confined within the NSSL. Given solar-like input parameters, a detailed calculation shows that the MRI should operate with latitudinal field strengths up to about 1,000 G (Methods).

Background shear modification dominates the MRI saturation mechanism (Methods), roughly

$$|\Omega'|^2 \approx \frac{H_r^2}{R_\odot^2} \frac{(2\Omega S - \omega_A^2)(S^2 + \omega_A^2)^2}{2\Omega(S + 2\Omega)(S^2 + (2\Omega)^2 + 2\omega_A^2)}, \quad (3)$$

where Ω' represents the dynamic changes in differential rotation. For $S \approx \Omega \approx \omega_A$, $|\Omega'| \approx 7$ nHz, roughly consistent with the observed torsional oscillation amplitude (Fig. 1d).

We compute a suite of growing global perturbations using Dedalus²⁵ to model the initial phase of the solar cycle with quasi-realistic solar input parameters (Methods). Figure 2 shows representative solutions.

We find two distinct cases: (1) a fast branch with direct growth rates, γ , comparable to a priori estimates and (2) a slow branch with longer but relevant growth times and oscillation periods. The eigenmodes are confined to the NSSL, reaching from the surface to $r/R_\odot \approx 0.90$ – 0.95 , at which point the background shear becomes MRI stable.

For case 1, $\gamma/\Omega_0 \approx 6 \times 10^{-2}$ (given $\Omega_0 = 466$ nHz) with corresponding e-folding time, $t_e \approx 60$ days and no discernible oscillation frequency. The pattern comprises roughly one wave period between the equator and about 20° latitude, similar to the rotation perturbations seen in the torsional oscillations.

For case 2, $\gamma/\Omega_0 \approx 6 \times 10^{-3}$ with $t_e \approx 600$ days and oscillation frequency $\omega/\Omega_0 \approx 7 \times 10^{-3}$, corresponding to a period $P \approx 5$ years. The pattern comprises roughly one wave period between the equator and about 20° – 30° latitude.

Apart from cases 1 and 2, we find 34 additional purely growing fast-branch modes, two additional oscillatory modes and one intermediate exceptional mode (Extended Data Figs. 1–3).

Using the full numerical MHD eigenstates, we compute a systematic estimate for the saturation amplitude using quasi-linear theory (Methods): $|\Omega'| \approx 6$ nHz for case 1 and $|\Omega'| \approx 3$ nHz for case 2; both comparable to the observed torsional oscillation amplitude and the simple analytical estimates from equation (3). The true saturated state would comprise an interacting superposition of the full spectrum of modes.

Notably, the slow-branch current helicity, $\mathcal{H} \propto \mathbf{b} \cdot \nabla \times \mathbf{b}$, follows the hemispherical sign rule¹⁰, with $\mathcal{H} < 0$ in the north and $\mathcal{H} > 0$ in the south. The slow-branch modes seem to be rotationally constrained, consistent with their low Rossby number²⁶, providing a pathway for understanding the helicity sign rule.

Further helioseismic data analyses could test our predictions. The MRI would not operate if the poloidal field is too strong, nor would it explain the torsional oscillations if it is too weak. We predict correlations between the flow perturbations and magnetic fields, which time-resolved measurements could test, constraining joint helioseismic inversions of flows and magnetic fields.

An MRI-driven dynamo may also explain the formation and cessation of occasional grand minima²⁷ (for example, Maunder). As an essentially nonlinear dynamo, the MRI is not a traditional kinematic dynamo starting from an infinitesimal seed field on each new cycle (Methods). Rather, a moderate poloidal field exists at the solar minimum, and the MRI processes it into a toroidal configuration. If the self-sustaining poloidal-to-toroidal regeneration sometimes happens imperfectly, then subsequent solar cycles could partially fizzle, leading to weak subsurface fields and few sunspots. Eventually, noise could push the system back onto its normal cyclic behaviour, as in the El Niño Southern Oscillation²⁸.

Finally, our simulations intentionally contain reduced physics to isolate the MRI as an important agent in the dynamo process, filtering out large-scale baroclinic effects, small-scale convection and nonlinear dynamo feedback. Modelling strong turbulent processes is arduous: turbulence can simultaneously act as dissipation, drive large-scale flows such as the NSSL, produce mean electromotive forces and excite collective instabilities. Although sufficiently strong turbulent dissipation could eventually erase all large-scale dynamics, the mere presence of the solar torsional oscillations implies much can persist within the roiling background.


Online content

Any methods, additional references, Nature Portfolio reporting summaries, source data, extended data, supplementary information, acknowledgements, peer review information; details of author contributions and competing interests; and statements of data and code availability are available at <https://doi.org/10.1038/s41586-024-07315-1>.

1. Maunder, E. W. The Sun and sunspots, 1820–1920. (plates 13, 14, 15, 16.). *Mon. Not. R. Astron. Soc.* **82**, 534–543 (1922).
2. Snodgrass, H. B. & Howard, R. Torsional oscillations of the Sun. *Science* **228**, 945–952 (1985).
3. Vorontsov, S. V., Christensen-Dalsgaard, J., Schou, J., Strakhov, V. N. & Thompson, M. J. Helioseismic measurement of solar torsional oscillations. *Science* **296**, 101–103 (2002).
4. Hathaway, D. H., Upton, L. A. & Mahajan, S. S. Variations in differential rotation and meridional flow within the Sun's surface shear layer 1996–2022. *Front. Astron. Space Sci.* **9**, 1007290 (2022).

5. Chandrasekhar, S. The stability of non-dissipative Couette flow in hydromagnetics. *Proc. Natl Acad. Sci. USA* **46**, 253–257 (1960).
6. Balbus, S. A. & Hawley, J. F. A powerful local shear instability in weakly magnetized disks. I – Linear analysis. *Astrophys. J.* **376**, 214 (1991).
7. Wang, Y., Gilson, E. P., Ebrahimi, F., Goodman, J. & Ji, H. Observation of axisymmetric standard magnetorotational instability in the laboratory. *Phys. Rev. Lett.* **129**, 115001 (2022).
8. Parker, E. N. A solar dynamo surface wave at the interface between convection and nonuniform rotation. *Astrophys. J.* **408**, 707 (1993).
9. Baldner, C. S., Antia, H. M., Basu, S. & Larson, T. P. Solar magnetic field signatures in helioseismic splitting coefficients. *Astrophys. J.* **705**, 1704–1713 (2009).
10. Pevtsov, A. A., Canfield, R. C. & Metcalf, T. R. Latitudinal variation of helicity of photospheric magnetic fields. *Astrophys. J. Lett.* **440**, L109 (1995).
11. Babcock, H. W. The topology of the Sun's magnetic field and the 22-year cycle. *Astrophys. J.* **133**, 572 (1961).
12. Karak, B. B. & Miesch, M. Solar cycle variability induced by tilt angle scatter in a Babcock-Leighton solar dynamo model. *Astrophys. J.* **847**, 69 (2017).
13. Vasil, G. M. & Brummell, N. H. Constraints on the magnetic buoyancy instabilities of a shear-generated magnetic layer. *Astrophys. J.* **690**, 783–794 (2009).
14. Howe, R. Solar rotation. In *Astrophysics and Space Science Proc.* Vol. 57 (eds Monteiro, M. et al.) 63–74 (Springer, 2020).
15. Cattaneo, F. & Hughes, D. W. Dynamo action in a rotating convective layer. *J. Fluid Mech.* **553**, 401–418 (2006).
16. Chen, R. & Zhao, J. A comprehensive method to measure solar meridional circulation and the center-to-limb effect using time-distance helioseismology. *Astrophys. J.* **849**, 144 (2017).
17. Nelson, N. J., Brown, B. P., Brun, A. S., Miesch, M. S. & Toomre, J. Buoyant magnetic loops in a global dynamo simulation of a young sun. *Astrophys. J. Lett.* **739**, L38 (2011).
18. Käpylä, P. J., Käpylä, M. J. & Brandenburg, A. Confirmation of bistable stellar differential rotation profiles. *Astron. Astrophys.* **570**, A43 (2014).
19. Hotta, H. & Kusano, K. Solar differential rotation reproduced with high-resolution simulation. *Nat. Astron.* **5**, 1100–1102 (2021).
20. Brandenburg, A. The case for a distributed solar dynamo shaped by near-surface shear. *Astrophys. J.* **625**, 539–547 (2005).
21. Dikpati, M., Corbard, T., Thompson, M. J. & Gilman, P. A. Flux transport solar dynamos with near-surface radial shear. *Astrophys. J.* **575**, L41–L45 (2002).
22. Vasil, G. M. On the magnetorotational instability and elastic buckling. *Proc. R. Soc. A Math. Phys. Eng. Sci.* **471**, 20140699 (2015).
23. Oishi, J. S. et al. The magnetorotational instability prefers three dimensions. *Proc. R. Soc. A Math. Phys. Eng. Sci.* **476**, 20190622 (2020).
24. Kagan, D. & Wheeler, J. C. The role of the magnetorotational instability in the sun. *Astrophys. J.* **787**, 21 (2014).
25. Burns, K. J., Vasil, G. M., Oishi, J. S., Lecoanet, D. & Brown, B. P. Dedalus: a flexible framework for numerical simulations with spectral methods. *Phys. Rev. Res.* **2**, 023068 (2020).
26. Vasil, G. M., Julien, K. & Featherstone, N. A. Rotation suppresses giant-scale solar convection. *Proc. Natl Acad. Sci. USA* **118**, e2022518118 (2021).
27. Eddy, J. A. The Maunder minimum: the reign of Louis XIV appears to have been a time of real anomaly in the behavior of the sun. *Science* **192**, 1189–1202 (1976).
28. Suarez, M. J. & Schopf, P. S. A delayed action oscillator for ENSO. *J. Atmos. Sci.* **45**, 3283–3287 (1988).
29. Larson, T. P. & Schou, J. Global-mode analysis of full-disk data from the Michelson Doppler Imager and the Helioseismic and Magnetic Imager. *Solar Phys.* **293**, 29 (2018).

Publisher's note Springer Nature remains neutral with regard to jurisdictional claims in published maps and institutional affiliations.

 **Open Access** This article is licensed under a Creative Commons Attribution 4.0 International License, which permits use, sharing, adaptation, distribution and reproduction in any medium or format, as long as you give appropriate credit to the original author(s) and the source, provide a link to the Creative Commons licence, and indicate if changes were made. The images or other third party material in this article are included in the article's Creative Commons licence, unless indicated otherwise in a credit line to the material. If material is not included in the article's Creative Commons licence and your intended use is not permitted by statutory regulation or exceeds the permitted use, you will need to obtain permission directly from the copyright holder. To view a copy of this licence, visit <http://creativecommons.org/licenses/by/4.0/>.

© The Author(s) 2024

Methods

Numerical calculations

We solve for the eigenstates of the linearized anelastic MHD equations^{30,31} in spherical-polar coordinates $(r, \theta, \phi) = (\text{radius, colatitude, longitude})$. Using $R_\odot = 6.96 \times 10^{10}$ cm for the solar radius, we simulate radii between $r_0 \leq r \leq r_1$ where $r_0/R_\odot = 0.89$ and $r_1/R_\odot = 0.99$. We place the top of the domain at 99% because several complicated processes quickly increase in importance between this region and the photosphere (for example, partial ionisation, radiative transport and much stronger convection effects). We use the anelastic MHD equations in an adiabatic background to capture the effects of density stratification on the background Alfvén velocities (density varies by roughly a factor of 100 across the NSSL, causing about a factor of 10 change in Alfvén speed) and asymmetries in velocity structures introduced by the density stratification by $\nabla \cdot (\rho \mathbf{u})$. A key aspect of the anelastic approximation is that all entropy perturbations must be small, which is reasonable in the NSSL below $0.99R_\odot$. We do not use the fully compressible equations, as these linear instability modes do not have acoustic components. Future MRI studies incorporating buoyancy effects (for example, the deep MRI branches at high latitudes) should use a fully compressible (but low Mach number) model³².

Input background parameters. We include density stratification using a low-order polynomial approximation to the Model-S profile³³. In units of g cm^{-3} , with $h = (r - r_0)/(r_1 - r_0)$,

$$\rho_0 = \alpha_0 - \alpha_1 h + \alpha_2 h^2 - \alpha_3 h^3 + \alpha_4 h^4, \quad (4)$$

$$\alpha_0 = 0.031256, \quad (5)$$

$$\alpha_1 = 0.053193, \quad (6)$$

$$\alpha_2 = 0.033703, \quad (7)$$

$$\alpha_3 = 0.023766, \quad (8)$$

$$\alpha_4 = 0.012326, \quad (9)$$

which fits the Model-S data to better than 1% within the computational domain. The density at $h = 1$ is $\rho_0 = 0.000326$ compared with 0.031256 at $h = 0$.

The density profile is close to an adiabatic polytrope with r^{-2} gravity and $5/3$ adiabatic index. An adiabatic background implies that buoyancy perturbations diffuse independently of the MHD and decouple from the system.

We use a low-degree polynomial fit to the observed NSSL differential rotation profile. For $\mu = \cos(\theta)$,

$$\mathbf{u}_0 = \Omega(r, \theta) r \sin(\theta) \mathbf{e}_\phi, \quad (10)$$

$$\Omega(r, \theta) = \Omega_0 R(h) \Theta(\mu), \quad (11)$$

where $\Omega_0 = 466 \text{ nHz} \approx 2.92 \times 10^{-6} \text{ s}^{-1}$ and

$$R(h) = 1 + 0.02 h - 0.01 h^2 - 0.03 h^3, \quad (12)$$

$$\Theta(\mu) = 1 - 0.145 \mu^2 - 0.148 \mu^4. \quad (13)$$

We use the angular fit from ref. 34. The radial approximation results from fitting the equatorial profile from ref. 29 shown in Fig. 1a. Below 60° latitude, the low-degree approximation agrees with the

full empirical profile to within 1.25%. The high-latitude differential rotation profile is less constrained because of observational uncertainties.

We define the background magnetic field in terms of a vector potential,

$$\mathbf{B}_0 = \nabla \times \mathbf{A}_0, \quad (14)$$

$$\mathbf{A}_0 = \frac{B(r)}{2} r \sin(\theta) \mathbf{e}_\phi, \quad (15)$$

where

$$B(r) = B_0 ((r/r_1)^{-3} - (r/r_1)^2), \quad (16)$$

and $B_0 = 90$ G. The r^{-3} term represents a global dipole. The r^2 term represents a field with a similar structure but containing electric current,

$$\mathbf{J}_0 = \frac{\nabla \times \mathbf{B}_0}{4\pi} = \frac{5B_0}{4\pi r_1^2} r \sin(\theta) \mathbf{e}_\phi. \quad (17)$$

The background field is in MHD force balance,

$$\mathbf{J}_0 \times \mathbf{B}_0 = \nabla(\mathbf{A}_0 \cdot \mathbf{J}_0). \quad (18)$$

The MHD force balance generates magnetic pressure, which inevitably produces entropy, s' , and enthalpy, h' , perturbations using

$$\frac{\nabla(\mathbf{A}_0 \cdot \mathbf{J}_0)}{\rho_0} + T_0 \nabla s' = \nabla h', \quad (19)$$

where

$$s' = \frac{1}{\Gamma_3 - 1} \frac{\mathbf{A}_0 \cdot \mathbf{J}_0}{T_0 \rho_0}, \quad h' = \frac{\Gamma_3}{\Gamma_3 - 1} \frac{\mathbf{A}_0 \cdot \mathbf{J}_0}{\rho_0}, \quad (20)$$

and Γ_3 is the third adiabatic index. However, the MRI is a weak-field instability, implying magnetic buoyancy and baroclinicity effects are subdominant. For the work presented here, we neglect the contributions of magnetism to entropy (magnetic buoyancy) and consider adiabatic motions. We expect this to be valid for MRI in the NSSL, but studies of MRI in the deep convection zone at high latitudes would need to incorporate these neglected effects.

We choose our particular magnetic field configuration rather than a pure dipole because the radial component $\mathbf{e}_r \cdot \mathbf{B}_0 = B(r) \cos(\theta)$ vanishes at $r = r_1$. The poloidal field strength in the photosphere is about 1 G, but measurements suggest sub-surface field strengths of about 50–150 G (ref. 9). The near-surface field should exhibit a strong horizontal (as opposed to radial) character. Magnetic pumping³⁵ by surface granulation within the outer 1% of the solar envelope could account for filtering the outward radial field, with sunspot cores being prominent exceptions.

We also test pure dipoles and fields with an approximately 5% dipole contribution, yielding similar results. Furthermore, we test that the poloidal field is stable to current-driven instabilities. Our chosen confined field also has the advantage that $\mathbf{e}_\theta \cdot \mathbf{B}_0$ is constant to within 8% over $r_0 < r < r_1$. However, a pure dipole varies by about 37% across the domain. The RMS field amplitude is $|\mathbf{B}|_{\text{RMS}} \approx 2B_0 = 180$ G, about 25% larger than the maximum-reported inferred dipole equivalent⁹. However, projecting our field onto a dipole template gives an approximately 70 G equivalent at the $r = r_1$ equator. Overall, the sub-surface field is the least constrained input to our calculations, the details of which change over several cycles.

Article

Model equations. Respectively, the linearized anelastic momentum, mass-continuity and magnetic induction equations are

$$\rho_0(\partial_t \mathbf{u} + \boldsymbol{\omega}_0 \times \mathbf{u} + \boldsymbol{\omega} \times \mathbf{u}_0 + \nabla \bar{w}) = \nu \nabla \cdot (\rho_0 \boldsymbol{\sigma}) + \mathbf{j} \times \mathbf{B}_0 + \mathbf{J}_0 \times \mathbf{b}, \quad (21)$$

$$\nabla \cdot (\rho_0 \mathbf{u}) = 0, \quad (22)$$

$$\partial_t \mathbf{b} - \eta \nabla^2 \mathbf{b} = \nabla \times (\mathbf{u}_0 \times \mathbf{b} + \mathbf{u} \times \mathbf{B}_0), \quad (23)$$

where the traceless strain rate

$$\boldsymbol{\sigma} = \nabla \mathbf{u} + (\nabla \mathbf{u})^\top - \frac{2}{3} \nabla \cdot \mathbf{u} \mathbf{I}. \quad (24)$$

To find eigenstates, $\partial_t \rightarrow \gamma + i\omega$, where γ is the real-valued growth rate, and ω is a real-valued oscillation frequency. The induction equation (23) automatically produces MRI solutions satisfying $\nabla \cdot \mathbf{b} = 0$.

Given the velocity perturbation, \mathbf{u} , the vorticity $\boldsymbol{\omega} = \nabla \times \mathbf{u}$. Given the magnetic field (Gauss in cgs units), the current density perturbations $\mathbf{j} = \nabla \times \mathbf{b} / 4\pi$. At linear order, the Bernoulli function $\bar{w} = \mathbf{u}_0 \cdot \mathbf{u} + h'$, where h' represents enthalpy perturbations²⁶.

The velocity perturbations are impenetrable ($u_r = 0$) and stress-free ($\sigma_{r\theta} = \sigma_{r\phi} = 0$) at both boundaries. For the magnetic field, we enforce perfect conducting conditions at the inner boundary ($b_r = \partial_\theta b_\theta = \partial_\phi b_\phi = 0$). At the outer boundary, we test three different choices in common usage, as different magnetic boundary conditions have different implications for magnetic helicity fluxes through the domain, and these can affect global dynamo outcomes³⁶. Two choices with zero helicity flux are perfectly conducting and vacuum conditions, and we find only modest differences in the results. We also test a vertical field or open boundary (that is, $\partial_r b_r = b_\theta = b_\phi = 0$), which, although non-physical, explicitly allows a helicity flux. These open systems also had essentially the same results as the other two for growth rates and properties of eigenfunctions. We conduct most of our experiments using perfectly conducting boundary conditions, which we prefer on the same physical grounds as the background field.

We set constant and kinematic viscous and magnetic diffusivity parameters $\nu = \eta = 10^{-6}$ in units where $\Omega_0 = R_0 = 1$. The magnetic Prandtl number $\nu/\eta = \text{Pm} = 1$ assumes equal transport of vectors by the turbulent diffusivities. A more detailed analysis of the shear Reynolds numbers yields $\text{Re} = \text{Rm} = U_0 L_0 / \nu \approx 1,500$, where $U_0 \approx 5,000 \text{ cm s}^{-1}$ is the maximum shear velocity jump across the NSSL and $L_0 \approx 0.06 R_0$ is the distance between minimum and maximum shear velocity (see section ‘NSSL energetics and turbulence parameterization’ below).

We compute the following scalar-potential decompositions a posteriori,

$$\mathbf{u} = u_\phi \mathbf{e}_\phi + \frac{1}{\rho_0} \nabla \times (\rho_0 \psi \mathbf{e}_\phi), \quad (25)$$

$$\mathbf{b} = b_\phi \mathbf{e}_\phi + \nabla \times (a_\phi \mathbf{e}_\phi), \quad (26)$$

where both the magnetic scalar potential, a_ϕ , and the streamfunction, ψ , vanish at both boundaries.

We, furthermore, compute the current helicity correlation relative to global RMS values,

$$\mathcal{H} = \frac{\mathbf{b} \cdot \mathbf{j}}{|\mathbf{b}|_{\text{RMS}} |\mathbf{j}|_{\text{RMS}}}. \quad (27)$$

There is no initial helicity in the background poloidal magnetic field,

$$\mathbf{B}_0 = \nabla \times (A_0(r, \theta) \mathbf{e}_\phi) \Rightarrow \mathbf{B}_0 \cdot (\nabla \times \mathbf{B}_0) = 0.$$

Linear dynamical perturbations, $\mathbf{b}(r, \theta)$, will locally align with the background field and current. However, because the eigenmodes are wave-like, these contributions vanish exactly when averaged over hemispheres.

$$\langle \mathbf{b} \cdot (\nabla \times \mathbf{B}_0) \rangle = \langle \mathbf{B}_0 \cdot (\nabla \times \mathbf{b}) \rangle = 0.$$

The only possible hemispheric contributions arise when considering quadratic mode interactions,

$$\langle \mathbf{b} \cdot (\nabla \times \mathbf{b}) \rangle \neq 0.$$

This order is the first for which we could expect a non-trivial signal.

Finally, we also solve the system using several different mathematically equivalent equation formulations (for example, using a magnetic vector potential $\mathbf{b} = \nabla \times \mathbf{a}$, or dividing the momentum equations by ρ_0). In all cases, we find excellent agreement in the converged solutions. We prefer this formulation because of satisfactory numerical conditioning as parameters become more extreme.

Computational considerations. The Dedalus code²⁵ uses general tensor calculus in spherical-polar coordinates using spin-weighted spherical harmonics in (θ, ϕ) (refs. 37,38). For the finite radial shell, the code uses a weighted generalized Chebyshev series with sparse representations for differentiation, radial geometric factors and non-constant coefficients (for example, $\rho_0(r)$). As the background magnetic field and the differential rotation are axisymmetric and they contain only a few low-order separable terms in latitude and radius, these two-dimensional non-constant coefficients have a low-order representation in a joint expansion of spin-vector harmonics and Chebyshev polynomials. The result is a two-dimensional generalized non-Hermitian eigenvalue problem $Ax = \lambda Bx$, where x represents the full system spectral-space state vector. The matrices, A and B , are spectral-coefficient representations of the relevant linear differential and multiplication operators. Cases 1 and 2 use 384 latitudinal and 64 radial modes (equivalently spatial points). The matrices A and B remain sparse, with respective fill factors of about 8×10^{-4} and 4×10^{-5} .

The eigenvalues and eigenmodes presented here are converged to better than 1% relative absolute error (comparing 256 and 384 latitudinal modes). We also use two simple heuristics for rejecting poorly converged solutions. First, because λ_0 is complex valued, the resulting iterated solutions do not automatically respect Hermitian-conjugate symmetry, which we often find violated for spurious solutions. Second, the overall physical system is reflection symmetric about the equator, implying the solutions fall into symmetric and anti-symmetric classes. Preserving the desired parity is a useful diagnostic tool for rejecting solutions with mixtures of the two parities, which we check individually for each field quantity. The precise parameters and detailed implementation scripts are available at GitHub (https://github.com/geoffvasil/nssl_mri).

Analytic and semi-analytic estimates

Local equatorial calculation. Our preliminary estimates of the maximum poloidal field strength involve solving a simplified equatorial model of the full perturbation equations, setting the diffusion parameters $\nu, \eta \rightarrow 0$. Using a Lagrangian displacement vector, $\boldsymbol{\xi}$, in Eulerian coordinates

$$\mathbf{u} = \partial_t \boldsymbol{\xi} + \mathbf{u}_0 \cdot \nabla \boldsymbol{\xi} - \boldsymbol{\xi} \cdot \nabla \mathbf{u}_0, \quad (28)$$

$$\mathbf{b} = \nabla \times (\boldsymbol{\xi} \times \mathbf{B}_0). \quad (29)$$

In local cylindrical coordinates near the equator (r, ϕ, z) , we assume all perturbations are axis-symmetric and depend harmonically $\propto e^{i(k_{zz} - \omega t)}$. The cylindrical assumption simplifies the analytical

calculations while allowing a transference of relevant quantities from the more comprehensive spherical model. That is, we assume a purely poloidal background field with the same radial form as the full spherical computations, $\mathbf{B}_0 = B_z(r)\mathbf{e}_z$. We use the same radial density and angular rotation profiles, ignoring latitudinal dependence. The radial displacement, ξ_r , determines all other dynamical quantities,

$$\xi_\phi = -\frac{2i\omega}{\omega^2 - k_z^2 v_A^2} \xi_r, \quad (30)$$

$$\xi_z = \frac{i}{k_z r \rho_0} \frac{d(r\rho_0 \xi_r)}{dr} \quad (31)$$

$$\omega = v_A^2 \frac{B'_z}{B_z} \xi_r + \frac{\omega^2}{k_z^2 r \rho_0} \frac{d(r\rho_0 \xi_r)}{dr}, \quad (32)$$

where $v_A(r) = B_z(r)/\sqrt{4\pi\rho_0(r)}$. The radial momentum equation gives a second-order two-point boundary-value problem for $\xi_r(r)$. The resulting real-valued differential equation depends on ω^2 ; the instability transitions directly from oscillations to exponential growth when $\omega = 0$. We eliminate terms containing $\xi'_r(r)$ with the Liouville transformation $\Psi(r) = \sqrt{r} B_z(r) \xi_r(r)$. The system for the critical magnetic field reduces to a Schrödinger-type equation,

$$-\Psi''(r) + k_z^2 \Psi(r) + V(r) \Psi(r) = 0, \quad (33)$$

with boundary conditions

$$\Psi(r=r_0) = \Psi(r=r_1) = 0 \quad (34)$$

and potential,

$$V = \frac{r}{v_A^2} \frac{d\Omega^2}{dr} + \frac{r\rho_0}{B_z} \frac{d}{dr} \left(\frac{1}{r\rho_0} \frac{dB_z}{dr} \right) + \frac{3}{4r^2}. \quad (35)$$

Upper bound. The maximum background field strength occurs in the limit $k_z \rightarrow 0$. With fixed functional forms for $\Omega(r)$, $\rho_0(r)$, we suppose

$$B_z(r) = B_1 \frac{1 + 4(r/r_1)^5}{5(r/r_1)^3}, \quad (36)$$

with $B_1 = B_z(r_1)$ setting and overall amplitude and $1/B_1^2$ serving as a generalized eigenvalue parameter. We solve the resulting system with Dedalus using both Chebyshev and Legendre series for 64, 128 and 256 spectral modes, all yielding the same result, $B_1 = 1,070$ G. The results are also insensitive to detailed changes in the functional form of the background profile.

Growth rate. We use a simplified formula for the MRI exponential growth, proportional to $e^{\gamma t}$, in a regime not extremely far above onset²². That is,

$$\gamma^2 \approx \frac{\alpha^2 \omega_A^2 (2\Omega S - \omega_A^2 (1 + \alpha^2))}{\omega_A^2 + 4\Omega^2}, \quad (37)$$

where $\alpha = 2H/L \approx 0.2-0.3$ is the mode aspect ratio with latitudinal wavelength, $L \approx 20^\circ-30^\circ R_\odot$, and NSSL depth $H \approx 0.05 R_\odot$. The main text defines all other parameters. In the NSSL, $S \approx \Omega$. Therefore, $\gamma/\Omega \approx 0.1$, when $\alpha \approx 0.3$ and $\omega_A/\Omega \approx 1$; and $\gamma/\Omega \approx 0.01$, when $\alpha \approx 0.2$ and $\omega_A/\Omega \approx 0.1$.

Saturation amplitude. We use non-dissipative quasi-linear theory²² to estimate the amplitude of the overall saturation. In a finite-thickness

domain, the MRI saturates by transporting mean magnetic flux and angular momentum radially. Both quantities are (approximately) globally conserved; however, the instability shifts the magnetic flux inward and angular momentum outward, so the potential from equation (35) is positive everywhere in the domain.

Given the cylindrical radius, r , the local angular momentum and magnetic flux density

$$L = \rho_0 r u_\phi, \quad M = \rho_0 r a_\phi. \quad (38)$$

The respective local flux transport

$$\partial_t L + \nabla \cdot (L\mathbf{u}) = \nabla \cdot (r b_\phi \mathbf{b}), \quad (39)$$

$$\partial_t M + \nabla \cdot (M\mathbf{u}) = 0. \quad (40)$$

For quadratic-order feedback,

$$\partial_t(\rho_0 r^2 \delta u_\phi) = \partial_r(r^2(b_\phi b_r - \rho_0 u_\phi u_r)) + \partial_z(r^2(b_\phi b_z - \rho_0 u_\phi u_z)), \quad (41)$$

$$\partial_t(\rho_0 r^2 \delta a_\phi) = -\partial_r(r^2 \rho_0 a_\phi u_r) - \partial_z(r^2 \rho_0 a_\phi u_z). \quad (42)$$

For linear meridional perturbations,

$$u_r = -\partial_z \psi, \quad u_z = \frac{\partial_r(r\rho_0 \psi)}{r\rho_0}, \quad (43)$$

$$b_r = -\partial_z a_\phi, \quad b_z = \frac{\partial_r(r a_\phi)}{r}. \quad (44)$$

For the angular components,

$$\partial_t u_\phi = \partial_z \left((2\Omega - S) \psi + \frac{B_z}{4\pi\rho_0} b_\phi \right), \quad (45)$$

$$\partial_t a_\phi = \partial_z (B_z \psi), \quad (46)$$

$$\partial_t b_\phi = \partial_z (B_z u_\phi + S a_\phi). \quad (47)$$

Using the linear balances, we time integrate to obtain the latitudinal-mean rotational and magnetic feedback,

$$\delta\Omega = \frac{1}{r^3 \rho_0} \partial_r(r^2 \rho_0 \mathcal{L}), \quad (48)$$

$$\delta A = \frac{1}{r^2 \rho_0} \partial_r(r^2 \rho_0 \Phi). \quad (49)$$

where angle brackets represent z averages and

$$\mathcal{L} = \frac{2B_z \langle a_\phi u_\phi \rangle - (2\Omega - S) \langle a_\phi^2 \rangle}{2B_z^2}, \quad (50)$$

$$\Phi = \frac{\langle a_\phi^2 \rangle}{2B_z}. \quad (51)$$

The dynamic shear and magnetic corrections,

$$\delta S = -r \partial_r \delta\Omega, \quad \delta B_z = \frac{1}{r} \partial_r(r \delta A). \quad (52)$$

We derive an overall amplitude estimate by considering the functional

$$\mathcal{F} = \int (V|\psi|^2 + |\nabla\psi|^2) dr, \quad (53)$$

which results from integrating equation (33) with respect to $\Psi^*(r)$. The saturation condition is

$$\delta\mathcal{F} = -\mathcal{F}. \quad (54)$$

The left-hand side includes all linear-order perturbations in the potential, δV , and wavefunction, $\delta\psi$, where

$$\delta V = \frac{2r}{v_A^2} \frac{d(\Omega\delta\Omega)}{dr} - 2 \frac{\delta B_z}{B_z} \frac{r}{v_A^2} \frac{d\Omega^2}{dr} + \frac{r\rho_0}{B_z} \frac{d}{dr} \left(\frac{1}{r\rho_0} \frac{d\delta B_z}{dr} \right) - \frac{\delta B_z}{B_z} \frac{r\rho_0}{B_z} \frac{d}{dr} \left(\frac{1}{r\rho_0} \frac{dB_z}{dr} \right), \quad (55)$$

$$\delta\psi = \frac{\delta B_z}{B_z} \psi. \quad (56)$$

All reference and perturbation quantities derive from the full sphere numerical eigenmode calculation. We translate to cylindrical coordinates by approximating z averages with latitudinal θ averages. The spherical eigenmodes localize near the equator, and the NSSL thickness is only about 5% of the solar radius, justifying the cylindrical approximation in the amplitude estimate.

Empirically, the first δV term dominates the overall feedback calculation, owing to the shear corrections $\propto d\delta\Omega/dr - 1/H_r^2$. Isolating the shear effect produces the simple phenomenological formula in equation (3).

NSSL energetics and turbulence parameterization

We estimate that the order-of-magnitude energetics of the NSSL are consistent with the amplitudes of torsional oscillations. The torsional oscillations comprise $|\Omega'| \approx 1$ nHz rotational perturbation, relative to the $\Omega_0 \approx 466$ nHz equatorial frame rotation rate. However, the NSSL contains $\Delta\Omega \approx 11$ nHz mean rotational shear estimated from the functional form in equations (10)–(13). In terms of velocities, the shear in the NSSL has a peak contrast of roughly $U_0 \approx 5 \times 10^3$ cm s⁻¹ across a length scale $L_0 \approx 0.06R_\odot$. The relative amplitudes of the torsional oscillations to the NSSL background, $|\Omega'|/\Delta\Omega$, are thus about 10%. Meanwhile, the radial and latitudinal global differential rotations have amplitudes of the order of about 100 nHz. The relative energies are approximately the squares of these, implying that the Δ KE of the torsional oscillations is about 0.01% to the differential rotation and about 1% to the NSSL. These rough estimates show that the NSSL and the differential rotation can provide ample energy reservoirs for driving an MRI dynamo, and the amplitude of the torsional oscillations is consistent with nonlinear responses seen in classical convection-zone dynamos¹⁷.

Vigorous hydrodynamic convective turbulence probably establishes the differential rotation of the NSSL. The large reservoir of shear in the solar interior plays the analogue part of gravity and Keplerian shear in accretion disks. The details of solar convection are neither well understood nor well constrained by observations. There are indications, however, that the maintenance of the NSSL is separate from the solar cycle because neither the global differential rotation nor the NSSL shows substantial changes during the solar cycle other than in the torsional oscillations.

Strong dynamical turbulence in the outer layers of the Sun is an uncertainty of our MRI dynamo framework, but scale separation gives hope for progress. From our linear instability calculations, the solar MRI operates relatively close to the onset and happens predominantly on large scales. If the fast turbulence of the outer layers of the Sun acts

mainly as an enhanced dissipation, then the solar MRI should survive relatively unaffected. Treating scale-separated dynamics in this fashion has good precedent: large-scale baroclinic instability in the atmosphere of Earth gracefully ploughs through the vigorous moist tropospheric convection (thunderstorms). Scale-separated dynamics are particularly relevant because the MRI represents a type of essentially nonlinear dynamo, which cyclically reconfigures an existing magnetic field using kinetic energy as a catalyst. From previous work, it is clear that the deep solar convection zone can produce global-scale fields, but these fields generally have properties very different from the observed fields¹⁷. Essentially nonlinear MHD dynamos have analogues in pipe turbulence, and, similar to those systems, the self-sustaining process leads to an attractor in which the dynamo settles into a cyclic state independent of its beginnings.

A full nonlinear treatment of turbulence in the NSSL-MRI setting awaits future work. Here we adopt a simplified turbulence model using enhanced dissipation. To model the effects of turbulence, we assume that the viscous and magnetic diffusivities are enhanced such that the turbulent magnetic Prandtl number $Pm = 1$ (with no principle of turbulence suggesting otherwise). The momentum and magnetic Reynolds numbers are $Re = Rm \approx 1.5 \times 10^3$. These values are vastly more dissipative than the microphysical properties of solar plasma (that is, $Re \sim 10^{12}$), and the microphysical $Pm \ll 1$, implying that $Rm \ll Re$. The studies conducted here find relative independence in the MRI on the choices of Re within a modest range. By contrast, other instabilities (for example, convection) depend strongly on Re . We compute sample simulations down to $Re \approx 50$ with qualitatively similar results, although they match the observed patterns less well and require somewhat stronger background fields. Our adopted value of $Re \approx 1,500$ strikes a good balance for an extremely under-constrained process. Our turbulent parameterizations also produce falsifiable predictions: our proposed MRI dynamo mechanism would face severe challenges if future helioseismic studies of the Sun suggest that the turbulent dissipation is much larger than expected (for example, if the effective $Re \ll 1$). However, it is difficult to imagine how any nonlinear dynamics would happen in this scenario.

Data availability

The raw eigenfunction and eigenvalue data used to generate Fig. 2 can be found along with the analysis scripts at GitHub (https://github.com/geoffvasil/nssl_mri)³⁹.

Code availability

We use the Dedalus code and additional analysis tools written in Python, as noted and referenced in the Methods. Beyond the main Dedalus installation, all scripts are available at GitHub (https://github.com/geoffvasil/nssl_mri)³⁹.

30. Brown, B. P., Vasil, G. M. & Zweibel, E. G. Energy conservation and gravity waves in sound-proof treatments of stellar interiors. Part I. Anelastic approximations. *Astrophys. J.* **756**, 109 (2012).
31. Vasil, G. M., Lecoanet, D., Brown, B. P., Wood, T. S. & Zweibel, E. G. Energy conservation and gravity waves in sound-proof treatments of stellar interiors: II. Lagrangian constrained analysis. *Astrophys. J.* **773**, 169 (2013).
32. Anders, E. H. The photometric variability of massive stars due to gravity waves excited by core convection. *Nat. Astron.* **7**, 1228–1234 (2023).
33. Christensen-Dalsgaard, J. et al. The current state of solar modeling. *Science* **272**, 1286–1292 (1996).
34. Howe, R. Solar interior rotation and its variation. *Living Rev. Sol. Phys.* **6**, 1 (2009).
35. Tobias, S. M., Brummell, N. H., Clune, T. L. & Toomre, J. Transport and storage of magnetic field by overshooting turbulent compressible convection. *Astrophys. J.* **549**, 1183–1203 (2001).
36. Käpylä, P. J., Korpi, M. J. & Brandenburg, A. Open and closed boundaries in large-scale convective dynamos. *Astron. Astrophys.* **518**, A22 (2010).
37. Vasil, G. M., Lecoanet, D., Burns, K. J., Oishi, J. S. & Brown, B. P. Tensor calculus in spherical coordinates using Jacobi polynomials. Part-I: mathematical analysis and derivations. *J. Comput. Phys.* **X 3**, 100013 (2019).

38. Lecoanet, D., Vasil, G. M., Burns, K. J., Brown, B. P. & Oishi, J. S. Tensor calculus in spherical coordinates using Jacobi polynomials. Part-II: implementation and examples. *J. Comput. Phys.* **X 3**, 100012 (2019).
39. Vasil, G. et al. *GitHub* https://github.com/geoffvasil/nssl_mri (2024).

Acknowledgements D.L., K.A., K.J.B., J.S.O. and B.P.B. are supported in part by the NASA HTMS grant 80NSSC20K1280. D.L., K.J.B., J.S.O. and B.P.B. are partly supported by the NASA OSTFL grant 80NSSC22K1738. N.B. acknowledges support from the NASA grant 80NSSC22M0162. Computations were conducted with support from the NASA High-End Computing Program through the NASA Advanced Supercomputing (NAS) Division at Ames Research Center on the Pleiades supercomputer with allocation GID s2276. Our dear co-author, Keith Julien, passed away unexpectedly while this paper was in the press. We want to acknowledge the outstanding friend and colleague he was for so many years. He did much to make this work a reality and was thrilled to see it completed. He will be sorely missed.

Author contributions G.M.V., D.L., J.S.O. and K.J. conceived and designed the experiments. G.M.V. performed analytical and semi-analytical estimates. K.J.B. and D.L. developed the multidimensional spherical eigenvalue solver used in the computations. K.A. and D.L. performed and verified the eigenvalue computations. K.J.B., G.M.V., J.S.O., D.L. and B.P.B. contributed to the numerical simulation and analysis tools. G.M.V., D.L., B.P.B. and J.S.O. wrote and, along with K.J.B., K.A., K.J. and N.B., revised the paper. All authors participated in discussions around the experimental methods, results and the Article.

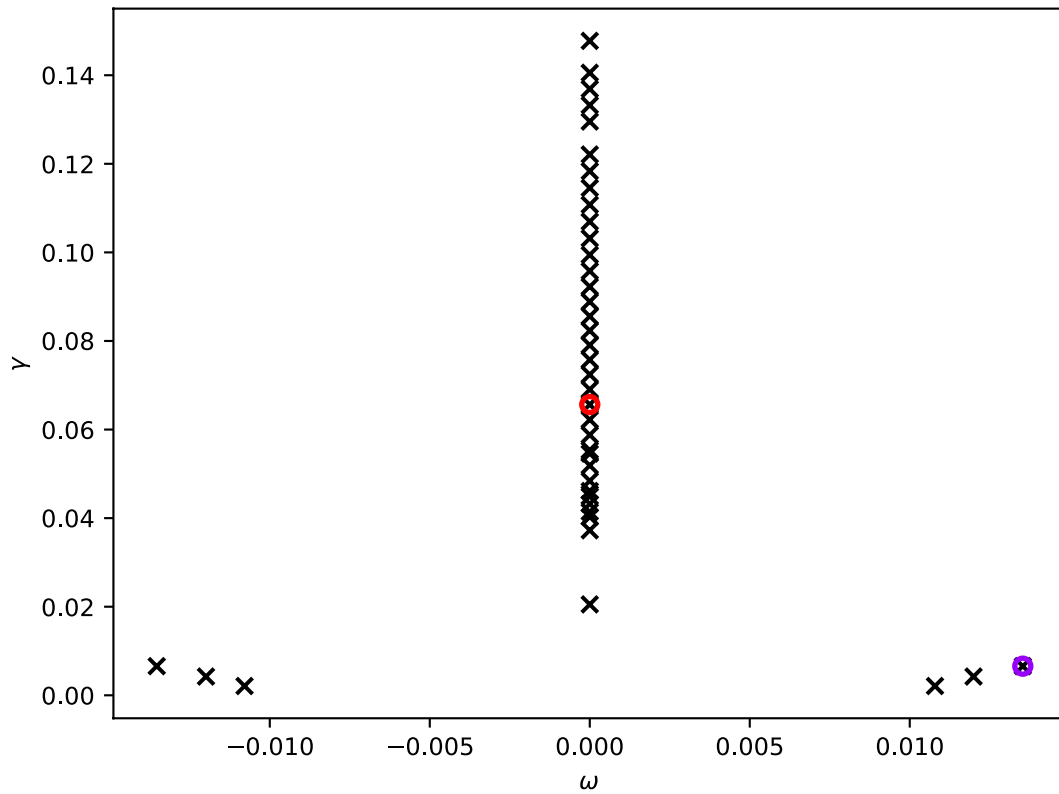
Competing interests The authors declare no competing interests.

Additional information

Correspondence and requests for materials should be addressed to Geoffrey M. Vasil.

Peer review information *Nature* thanks Steven Balbus and the other, anonymous, reviewer(s) for their contribution to the peer review of this work.

Reprints and permissions information is available at <http://www.nature.com/reprints>.

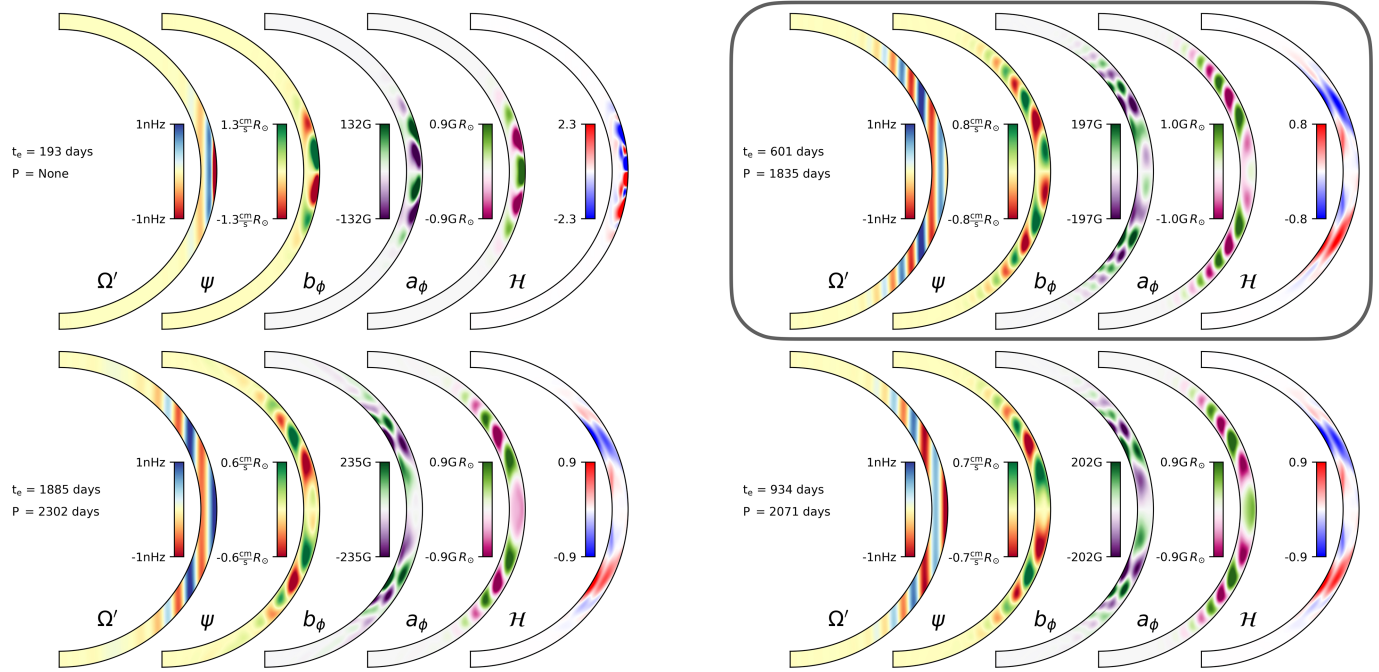


Extended Data Fig. 1 | Full diagram of complex-valued eigen-spectrum. The time dependence sends $\partial_t \rightarrow \gamma + i\omega$, with each real/imaginary component measured in terms of $\Omega_0 = 466$ nHz. The modes along the vertical axis appear to lie on a continuum, accumulating at a lower value. The isolate modes appear

to be point spectra. The red circle represents the case (i) “fast branch” from the main text. The purple circle (with its complex conjugate) represent the case (ii) presented “slow branch”.



Extended Data Fig. 2 | The complete collection of “fast branch” modes. The growth rates correspond to the vertical axis of Extended Data Fig. 1. Each case contains no discernible oscillations. For completeness, we show (boxed in grey) the $t_c = 60$ day fast-branch case (i) presented in the main text Fig. 2(a).



Extended Data Fig. 3 | The complete collection of “slow branch” modes. The growth rates correspond to the isolated spectrum in Extended Data Fig. 1. The upper-left image shows the point spectra along the vertical axis. The three

other images show the isolated oscillatory modes, including the slow-branch case (ii) mode (boxed in grey) presented in the main text Fig. 2(b).